This article may be downloaded for personal use only. Any other use requires prior permission of the author and AIP Publishing. This article appeared in Jiahao Wen, Changyong Liu, Shilong Zhang, Lei Zhou, Hui Tang, Yong Xia, Hongfu Zhang; Wake dynamics and coherence modes of vertical-axis wind turbines: The role of atmospheric boundary layer. Physics of Fluids 1 June 2025; 37 (6): 067123 and may be found at https://doi.org/10.1063/5.0271326.

Wake dynamics and coherence modes of vertical-axis wind turbines: the role of atmospheric boundary layer

Jiahao Wen (温嘉豪) [a]; Changyong Liu (刘昌永) [a*]; Shilong Zhang (张士龙) [a]; Lei Zhou (周蕾) [b,c]; Hui Tang (唐辉) [d]; Yong Xia (夏勇) [b]; Hongfu Zhang (张洪福) [d*]

[a] School of Civil Engineering, Harbin Institute of Technology, Harbin, 150090, China

[b] Department of Civil and Environmental Engineering, The Hong Kong Polytechnic University, Kowloon, Hong Kong, China

[c] School of Civil Engineering, Central South University, Changsha, 410083, China

[d] Department of Mechanical Engineering, The Hong Kong Polytechnic University, Kowloon, Hong Kong, China

*Corresponding authors

E-mail addresses: liuchangyong@hit.edu.cn (Changyong Liu); hongfu2233@126.com (Hongfu Zhang)

Abstract

Vertical axis wind turbines (VAWTs) are increasingly recognized as the preferred choice for large-scale wind energy harvesting, particularly in offshore environments, due to their unique advantages, including omni-directional capability and lower installation and maintenance costs. Variations in terrain and different phases of the diurnal cycle create distinct atmospheric boundary layer (ABL) conditions, which inevitably have a significant impact on the aerodynamic and wake characteristics of VAWTs. To systematically observe these effects, this study employs large eddy simulation to explore the influence of four representative ABL scenarios on VAWTs. The results indicate that ABL influences on VAWT aerodynamic performance are sensitive to installation height. ABLs with higher wind shear coefficients (WSCs) result in greater velocity deficits (VD) in near-wake regions, while turbulence intensity (TI) fluctuations increase with rising WSC. Higher installation heights facilitate a faster recovery of both VD and TI. Furthermore, vortex stability is affected by ABL conditions and installation height, as higher WSCs or lower heights bring unsteady vortex break positions closer to the rotor, thus enhancing turbulence. Modal decomposition reveals that the dominant mode frequency across various ABL conditions corresponds to twice the VAWT rotation frequency, highlighting the dynamic evolution of wake vortices. These findings provide valuable insights for the optimization of VAWT wind farm design, particularly in integrating ABL variability into the determination of hub height and turbine spacing strategies, thereby maximizing energy harvesting.

Keywords: Wind turbine wake; LES; ABL; VAWT; OMD

1. Introduction

Wind energy is a highly significant renewable energy source, whose sustainability, reliability, and high efficiency make it a compelling alternative to fossil fuel power generation schemes. Despite the existence of various devices for harvesting flow-energy [1-4], wind turbines serve as the primary means of wind energy harvesting [5-9]. Wind turbines are primarily categorized into vertical-axis wind turbines (VAWTs) and horizontal-axis wind turbines (HAWTs) [10]. In the past few decades, significant advancements have been made in HAWTs [11, 12], while the deployment of VAWTs has faced hindrances due to early incidents, resulting in a less favorable position compared to HAWTs [13]. Nevertheless, VAWTs have their distinct advantages [14, 15], including omni-directional capability, economical installation and maintenance expenses, etc. In the mid-2000s, there was renewed interest in the development of multi-megawatt VAWTs [13, 16], and various research institutions proposed several offshore floating VAWT concepts, including DeepWind [17].

In wind farms, the energy production of downstream turbines may be adversely affected by wake effects resulting from the presence of upstream wind turbines, leading to an average power loss of 10-20% [18]. However, the wake characteristics of VAWTs exhibit distinct differences compared to HAWTs [19]. For instance, the recovery of velocity deficit (VD) in the wake of VAWTs occurs at a significantly quicker rate compared to HAWTs [20]. Therefore, investigating the wake characteristics behind VAWTs is a crucial step in developing offshore VAWT wind farms. Unfortunately, research on wake effects in wind farms has predominantly focused on HAWTs [21], while studies related to VAWTs are still in their early stages [22].

Wind tunnel tests is a widely used approach for investigating the wake behavior of VAWTs. Tescione et al. [23] employed standard and stereoscopic particle image velocimetry (PIV) to examine the near wake of a VAWT. They found that compared with HAWT, the wake of VAWT exhibits intricate vorticity dynamics and a significant level of asymmetry. Peng et al. [24] determined the boundary between the near wake and mid-range wake of the VAWT based on wind tunnel test results. Araya et al. [25] demonstrated through PIV testing that enhanced rotor solidity results in a greater initial VD and a more rapid wake recovery, similar to the relative regularity of HAWTs [5].

The computational fluid dynamics (CFD) method is widely used to calculate and visualize the complex wake flow structures of VAWTs due to its powerful computational capabilities [26] and advanced post-processing functionalities [22]. The wake of an isolated VAWT was studied by Posa et al. [27] using large-eddy simulation (LES) at two different values of tip speed ratios (TSRs). The findings suggest that TSR is a critical parameter in determining the wake characteristics of VAWT, and an increase in TSR can enhance wake recovery. This phenomenon shows a resemblance to the TSR effect of HAWT's wake [7]. Kuang et al. [28] employed improved delayed detached eddy simulation to examine the wake characteristics of a VAWT, finding that inflows with higher turbulence intensity facilitate the recovery of wake VDs.

The atmospheric boundary layer (ABL) significantly influences the development of wind turbine wakes in wind farms, thereby affecting the fatigue loads and energy production of the turbines. The ABL flow effects on the wake characteristics of HAWTs has been sufficiently investigated owing to the significant development of HAWTs [29-32]. In recent years, the effects of ABL on VAWTs wake have started to draw attention [33-35]. Both Kadum et al. [33] and Rolin et al. [34] employed PIV testing to examine the wake of VAWT in ABL flow. However, their study did not consider the influence of ABL parameters on the wake characteristics. Hohman et al. [35] employed a PIV study of the wake in both uniform flow and ABL flow. The results indicate that the ABL inflow conditions significantly influence the wake behavior of the VAWT, such as reducing the strength and coherence of the wake vortices.

A review of the relevant literature reveals a clear gap in understanding the effects of ABL flows with varying wind shear exponents on the wake dynamics of VAWTs. Compared to uniform inflow conditions, ABL flows exert markedly different influences on the aerodynamic performance and wake characteristics of VAWTs. While it is well established that different ABL conditions significantly affect the energy output [36] and wake behavior [29] of HAWTs, their impact on VAWTs remains largely unexplored. With the growing interest in and deployment of large-scale VAWTs [37, 38], it is increasingly important to address this research gap in order to provide meaningful insights for the structural design of large VAWTs and the layout optimization of VAWT-based wind farms.

In this study, four typical wind shear coefficients (WSCs) are utilized to explore the influence of the ABL on the aerodynamic behavior and wake dynamics of the VAWT, employing mode decomposition methods to extract the coherent structures of the wake. In addition, the effects of ABL on VAWT installed at different heights above the sea level are also included. The organization of this paper is as follows: Section 2 details the VAWT geometry, the numerical simulation framework, and the mode decomposition techniques utilized. Subsequently, Section 3 introduces the effects of the ABL on the aerodynamic behavior and wake dynamics of the VAWT. Finally, Section 4 presents the main conclusions drawn from this study.

2. Numerical framework and mode decomposition techniques

2.1 Wind turbine model

This study employs a representative VAWT model [39], which has been widely adopted in previous research [40-46]. The scaled VAWT utilizes the NACA 0021 airfoil profile, with a chord length of 0.265 meters. The blades have a span of H=1.2m, and the rotor has a diameter of D=2m, as shown in Figs. 1(a) and 1(b). Additional details regarding the VAWT can be found in Ref. [39].

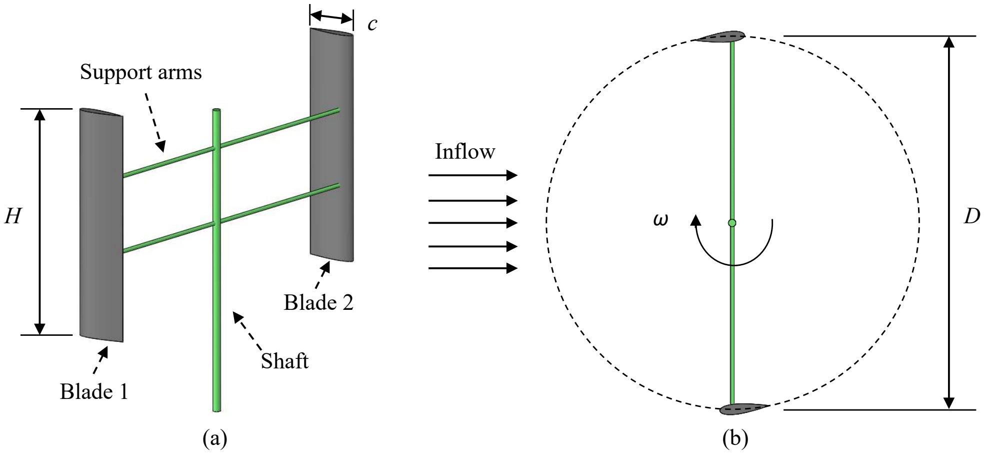

(a) (b)

Fig. 1. Schematic representations of the VAWT: (a) three-dimensional view and (b) two-dimensional view. [28].

The TSR (λ) of the VAWT is determined by the following equation:

$$\lambda = \frac{\omega D}{2U_0} \tag{1}$$

where ω represents the rotor's angular speed, D denotes the diameter of the rotor, and U_0 signifies the wind speed at the reference height.

The torque coefficient (C_T) and power coefficient (C_P) of the VAWT are defined by the following equations:

$$C_T = \frac{T}{\rho U_0^2 H D^2 / 4} \tag{2}$$

$$C_P = C_T \times \lambda \tag{3}$$

where T denotes the torque, ρ represents the air density, and H refers to the span length of the blade.

2.2 Computational domain and grid generation

The numerical computational domain is illustrated in Fig. 2. The domain is divided into two regions: a cylindrical region that rotates and a rectangular region that remains stationary. The cylindrical region surrounding the rotor has a diameter and height of 1.8*H* and 2*D* [28], respectively. The rotation of the rotor is realized using the sliding mesh technique.

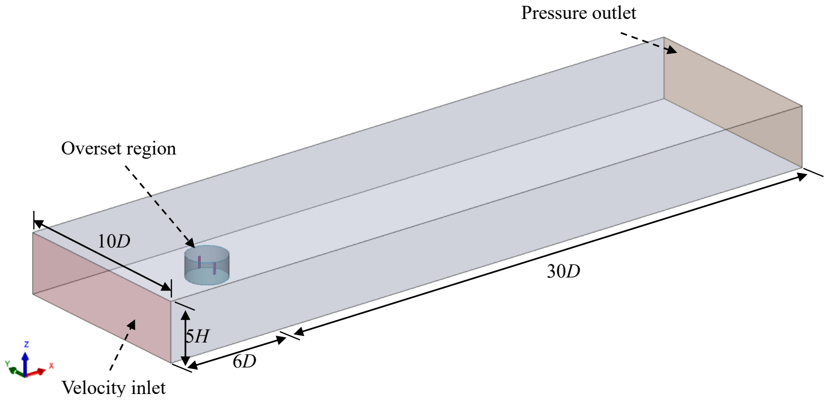

Fig. 2. Schematic of the computational domain.

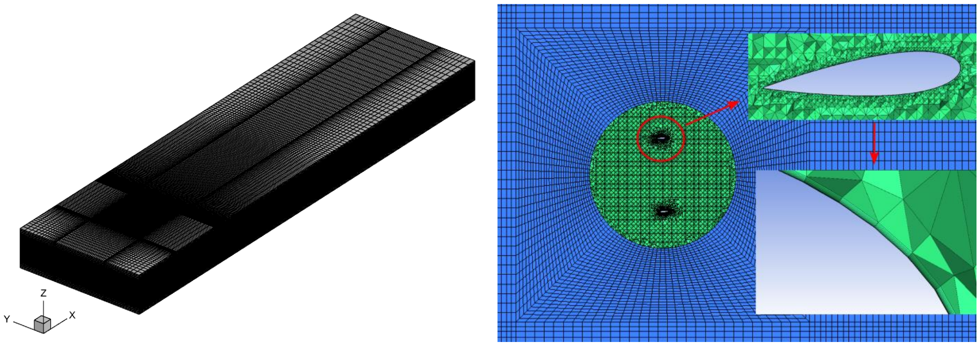

(a) (b)

Fig. 3. Grids in the domain: (a) global and (b) local.

To improve the calculation efficiency, the hexahedral grids in the stationary domain are progressively reduced in density along the streamwise direction (Fig. 3(a)) [5]. The grid distributions of the boundary layer surrounding the blades are shown in Fig. 3(b), which consist of 10 inflation layers with a normal direction spacing ratio of 1.2. In this study, the Reynolds number based on the airfoil chord, denoted as Re_c (where $\mathrm{Re}_c = U_c c / \nu$, with U_c is the relative velocity at the mid-span airfoil), ranges from 1.70×10^5 to 4.57×10^5. The height of the first grid layer on the airfoil surface is set to 1.6×10^{-5} m, to satisfy the requirements of $y^+ < 1$. The mesh configuration in the wake region follows the setups proposed by Zhang et al. [46] and Kuang et al. [28], ensuring that the grid meets the resolution requirements and provides a smooth transition across computational domains.

2.3 Boundary conditions and computational setup

The outlet of the computational domain is designated as a pressure outlet, while the inlet boundary condition is specified as a velocity inlet. The bottom of the domain and the VAWT are configured as non-slip walls, while the remaining boundaries of the domain are treated as symmetry conditions. In the grid independence test and numerical simulation accuracy verification, the inlet features a uniform flow with a velocity of 8 m/s. In subsequent studies, distinct velocity inlet profiles are defined based on the wind shear characteristics of various ABL inflows and implemented at the velocity inlet boundary using User Defined Functions (UDF). The wind shear of the ABL is characterized using the power law method, as expressed in the following equation:

$$U_z = U_{z_0}\left(\frac{z}{z_0}\right)^{\alpha} \tag{4}$$

where U_z is the wind speed at height z, and α denotes the wind shear coefficient (WSC). The study adopts various WSCs of α = 0.05, 0.15, 0.3 and 0.45, which represent the diurnal cycle of ABL from daytime to nighttime [36].The inflow velocity at the reference height z_0 ($z_0 = 2.5H$) is set to 8 m/s (U_{z_0}), as illustrated in Fig. 4.

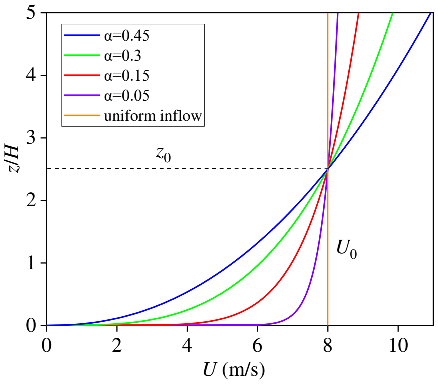

Fig. 4. Inlet streamwise wind velocity profiles under different ABL wind shear conditions.

This study employed LES utilizing the Smagorinsky–Lilly model, with the Smagorinsky constant set to 0.1 [47]. LES directly resolves turbulent vortices that have scales larger than the grid size while modeling smaller-scale vortices. The governing equations for the fluid are outlined below:

$$\frac{\partial \rho}{\partial t}+\frac{\partial}{\partial x_i}\left(\rho \bar{u}_i\right)=0 \tag{5}$$

$$\frac{\partial\left(\rho \bar{u}_i\right)}{\partial t}+\frac{\partial\left(\rho \overline{u_j u_i}\right)}{\partial x_j}=\frac{\partial \sigma_{ij}}{\partial x_j}-\frac{\partial \bar{p}}{\partial x_i}-\frac{\partial \tau_{ij}}{\partial x_j} \tag{6}$$

where $\bar{u}$ denotes the resolved velocity, σ represents the stress tensor and τ_{ij} refers to the subgrid scale stress, respectively. Additional details can be found in Ref. [47].

In the present numerical simulations, the SIMPLE algorithm and bounded central differencing scheme [48] are employed. Based on previous study [28], the numerical computations employ a fixed time step of 0.001 s, which corresponds to a 1° azimuthal rotation of the VAWT at a TSR of 2.19. This fixed time step is consistently used for all cases in the present study. The calculations are conducted using ANSYS FLUENT.

2.4 Numerical model validation

2.4.1 Grid independence validation

The case of uniform inflow at a TSR of 2.517 is employed for grid independence validation. As illustrated in Fig. 5(a), the predicted torque coefficients of the VAWT are compared across five mesh topologies with varying grid resolutions (3.20 million, 4.36 million, 5.51 million, 6.20 million, and 7.30 million elements). The higher resolution grids specifically refine the mesh in the rotating domain and the far-wake region to capture the flow dynamics more accurately. With increasing grid resolution, the torque coefficient exhibits gradual stabilization. Notably, the discrepancy in predicted torque between the grid resolutions of 6.20 million and 7.30 million elements is negligible, with a relative error of only 0.04%. Furthermore, Fig. 5 (b) provides the normalized velocity profiles at downstream distance of $x/D = 3$, obtained from different grid configurations. The results indicate that the velocity profiles predicted by Mesh 4 (6.20 million) and Mesh 2 (4.36 million) are in close agreement. However, when the grid resolution is reduced to 3.20 million elements (Mesh 1), significant discrepancies are observed in the predicted velocity profile. To achieve a balance between computational accuracy and efficiency, the grid composed of 6.20 million elements (Mesh 4) is selected for subsequent analysis.

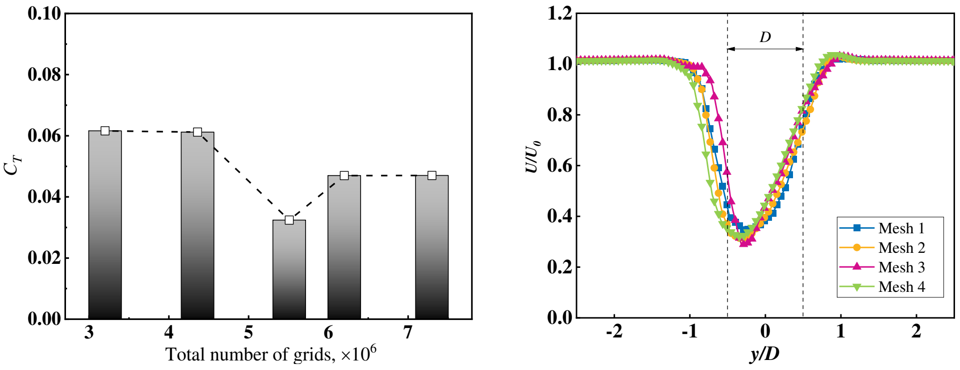

(a)

(b)

Fig. 5. Grid-independent test at TSR = 2.517. (a) torque coefficient, (b) mean velocity profiles at $x/D = 3$.

2.4.2 Solution accuracy validation

The predictions of the power coefficient at four different TSRs obtained from the CFD method are summarized in Table 1. The CFD results are in excellent agreement with the experimental results [39, 49], with the maximum relative error occurring at TSR = 0.740, measuring only 2.52%. Additionally, the wake velocity profile derived from the CFD method are compared with both experimental data and field measurements [39, 49], as illustrated in Fig. 6. From the figure, it is evident that both the wake width and the velocity variation trends predicted by the LES align well with the experimental results. The discrepancy near the centerline may result from the omission of the turbine support structure in the numerical model, which can locally alter the wake development and turbulence characteristics. Thus, the CFD simulation conducted in this study exhibits an acceptable level of reliability.

Table 1. Validation of the accuracy of power coefficient predictions.

TSR	LES	Experiments [39, 49]	Error (%)
0.740	0.0155	0.0159	2.52
1.240	0.0390	0.0400	2.50
1.734	0.1217	0.1224	0.57
2.517	0.1208	0.1220	0.98

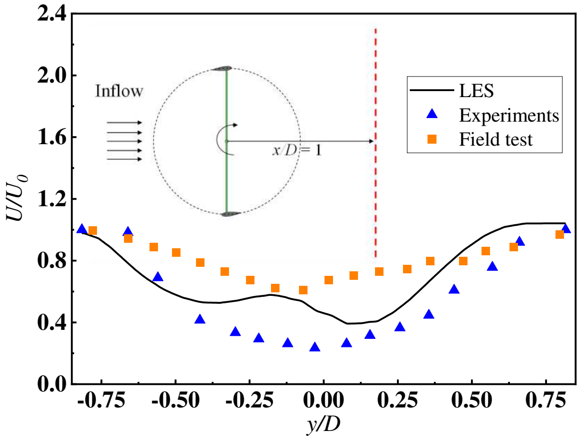

Fig. 6. Validation of the accuracy of wake prediction (TSR =2.19, x/D = 1).

2.5 Mode decomposition techniques

Modal decomposition techniques are powerful tools for extracting dominant coherent structures from unsteady flow fields, and have been widely applied in fluid mechanics and wind energy research [9, 50-52]. Dynamic mode decomposition (DMD) is a data-driven technique that decomposes unsteady flow fields into modes, each characterized by a distinct frequency and a specific growth or decay rate. In this study, we employ optimized mode decomposition (OMD), an advanced extension of the standard DMD approach. OMD utilizes an iterative procedure to identify the optimal combination of a linear model and modal subspace that minimizes the system's residual error, thereby enhancing the ability to capture the essential dynamics of nonlinear turbulent flows more effectively [53].

Leveraging the Koopman assumption, a linear operator (A) and a residual matrix (R) are introduced to map the 'before' snapshot matrix (U_{N-1}) to the 'after' matrix (U_N). This relationship can be expressed as follows:

$$AU_{N-1} = U_N + R \tag{7}$$

$$U_{N-1} = \left[u_1, u_2, u_3, \ldots, u_{N-1}\right] \tag{8}$$

$$U_N = \left[u_2, u_3, u_4, \ldots, u_N\right] \tag{9}$$

OMD determines the low-dimensional subspace by addressing an optimization problem designed to minimize the residual (R), thereby achieving the most accurate approximation of the mapping. The optimization problem and detailed algorithms are referenced in Ref. [53].

3. Results and discussion

3.1 ABL impact on aerodynamic performance

Four ABLs are considered, each characterized by a WSC, as shown in Fig. 4. The VAWT operates at approximately 167 revolutions per minute (RPM). Furthermore, various installation heights of the VAWT are examined to enhance the reliability of the conclusions.

The computational results of the C_p for the VAWT under varying WSC (α) and installation heights (h) are presented in Fig. 7. In this context, h represents the distance from the bottom of the blade to sea level, with values including 0.5H, 1H, 1.5H and 2H, where H is the span of the blade and $z_0 = 2.5H$. The incoming wind speed at the rotor hub is adopted to calculate the power coefficient of VAWT across these different installation heights. In Fig. 7, the results for uniform flow are depicted by solid lines, while the results for ABL under varying WSCs are illustrated by dashed lines. The discrepancies observed between the solid and dashed lines highlight the influence of ABL on the aerodynamic performance of VAWTs.

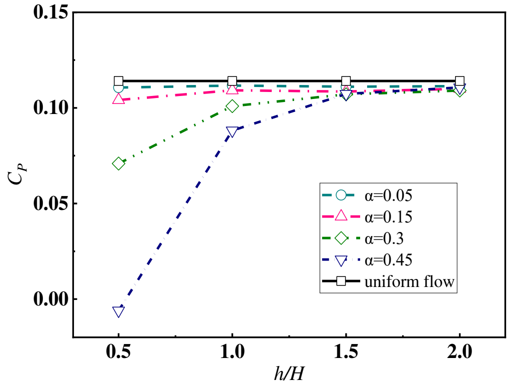

Fig. 7. Power coefficient (C_P) versus installation height (h) under different ABL conditions (TSR = 2.19). A general increasing trend in C_P with higher installation heights is observed, with the degree of sensitivity varying across ABL profiles.

As illustrated in Fig. 7, ABL significantly suppresses the aerodynamic performance of VAWTs, particularly at lower installation heights. For instance, when $h = H$, variations in the WSCs result in a reduction of the rotor's power coefficient, ranging from 4.36% to 37.84%. Notably, across all ABL scenarios, there is a consistent increase in the rotor's power coefficient with rising installation height. When h reaches 2H (where the hub height is z_0=2.5H), the variation in power coefficients among different ABL cases decreases to below 1%. These findings indicate that the impact of ABL on the aerodynamic performance of VAWTs is highly sensitive to installation height, with more pronounced differences among various ABL cases observed at lower heights.

Fig. 8 illustrates the fluctuations in torque output of the VAWT under various ABL conditions. As shown in Fig. 8(a), the torque curves for different WSCs exhibit stable behavior over time. However, it is evident that ABL influences the peak values of these torque curves. Specifically, for WSCs of 0.05, 0.15, 0.3, and 0.45, the corresponding peak torque values are 16.05, 13.59, 11.09, and 8.93, respectively. Notably, the peak values of the torque curves under ABL conditions are consistently lower than those observed under uniform flow conditions. This indicates that ABL adversely affects the torque output of the VAWT.

The fluctuating torque curve exhibits spectral characteristics that can be analyzed using the Fast Fourier Transform (FFT), which resolves time-dependent data into a summation of sine and cosine waves [47]. In this study, 5000 torque samples collected at each time step are used for the FFT analysis, with the results presented in Fig. 8(b). And the horizontal axis represents the normalized frequencies f/f_0, where f_0 is the rotating frequency of the rotor, and the vertical axis indicates the amplitude of these frequencies. The spectrum reveals the dominant frequency components of the torque curves along with their corresponding amplitudes. For WSC of 0.05, 0.15, 0.3 and 0.45, the first frequency components are all equal to $2f_0$, with corresponding amplitudes of 11.71, 10.28, 8.44, and 6.96, respectively. Notably, under ABL conditions, the amplitudes of both the first and third-order frequency components are smaller than those observed under uniform inflow conditions. Additionally, it is interesting to note that the second frequency components are all equal to $4f_0$, while the third frequency components correspond to $6f_0$.

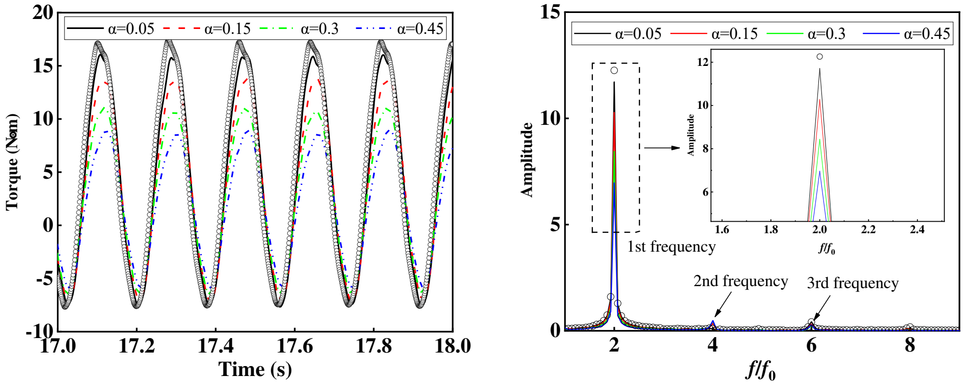

(a) (b)

Fig. 8. Torque output of the VAWT under different ABLs ($h = H$, scattered points denote uniform inflow conditions, TSR = 2.19): (a) time history curve, (b) spectrum.

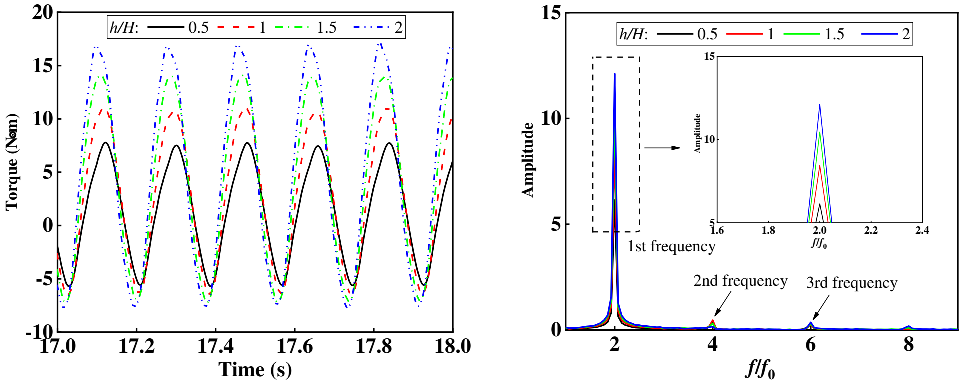

(a) (b)

Fig. 9. Torque output of the VAWT under different installation heights (α = 0.3, TSR = 2.19): (a) time history curve, (b) spectrum.

The fluctuations in torque output of the VAWT at various installation heights are presented in Fig. 9. The torque curves exhibit a behavior analogous to that observed under different ABL conditions, characterized by temporal stability, while the installation height influences the peak values of the torque curves. Specifically, as illustrated in Fig. 9(a), the peak torque values corresponding to installation heights of h/H = 0.5, 1, 1.5 and

2 are 7.78, 11.09, 13.96 and 16.94, respectively. The FFT analysis reveals that the first, second, and third frequency components for each installation height are consistently equal to $2f_0$, $4f_0$ and $6f_0$ respectively, as shown in Fig. 9(b). For the installation heights of $h/H = 0.5$, 1, 1.5 and 2, the corresponding amplitude of first frequency components are 6.14, 8.44, 10.46 and 12.12, respectively.

3.2 Wake characteristics

This subsection presents a detailed analysis of the wake dynamics of VAWTs under varying ABL conditions ($\alpha = 0.05$, 0.15, 0.3 and 0.45) with $h/H = 1$ and installation heights ($h/H = 0.5$, 1, 1.5 and 2) with $\alpha = 0.3$. The selection of $\alpha = 0.3$ is motivated by its predominance during diurnal cycles [36].

3.2.1 Effects of ABL

Fig. 10(a) depicts the horizontal normalized mean streamwise velocity profiles of the VAWT at various downstream locations, observed in the midspan section away from the shaft. The normalized mean streamwise velocity is defined as U/U_{hub}, where U_{hub} represents the inflow wind speed at the mid-span height of the blade. The coordinates along the axes are normalized with respect to the rotor diameter (D). As illustrated in Fig. 10(a), the horizontal width of the wake gradually increases with greater downstream distance across all ABL conditions. This expansion can be attributed to the displacement of coherent vortices within the wake towards the far-wake region, which enhances the exchange of momentum between the wake and the surrounding ambient air, thereby illustrating the inherent mechanism of wake development [28]. Additionally, the wake profiles display an asymmetric distribution, which is attributed to the Magnus effect [54]. As a result of this effect, a turning point in the wake evolution is observed near $y/D = -0.5$ at $x/D = 3$ in Fig. 10(a).

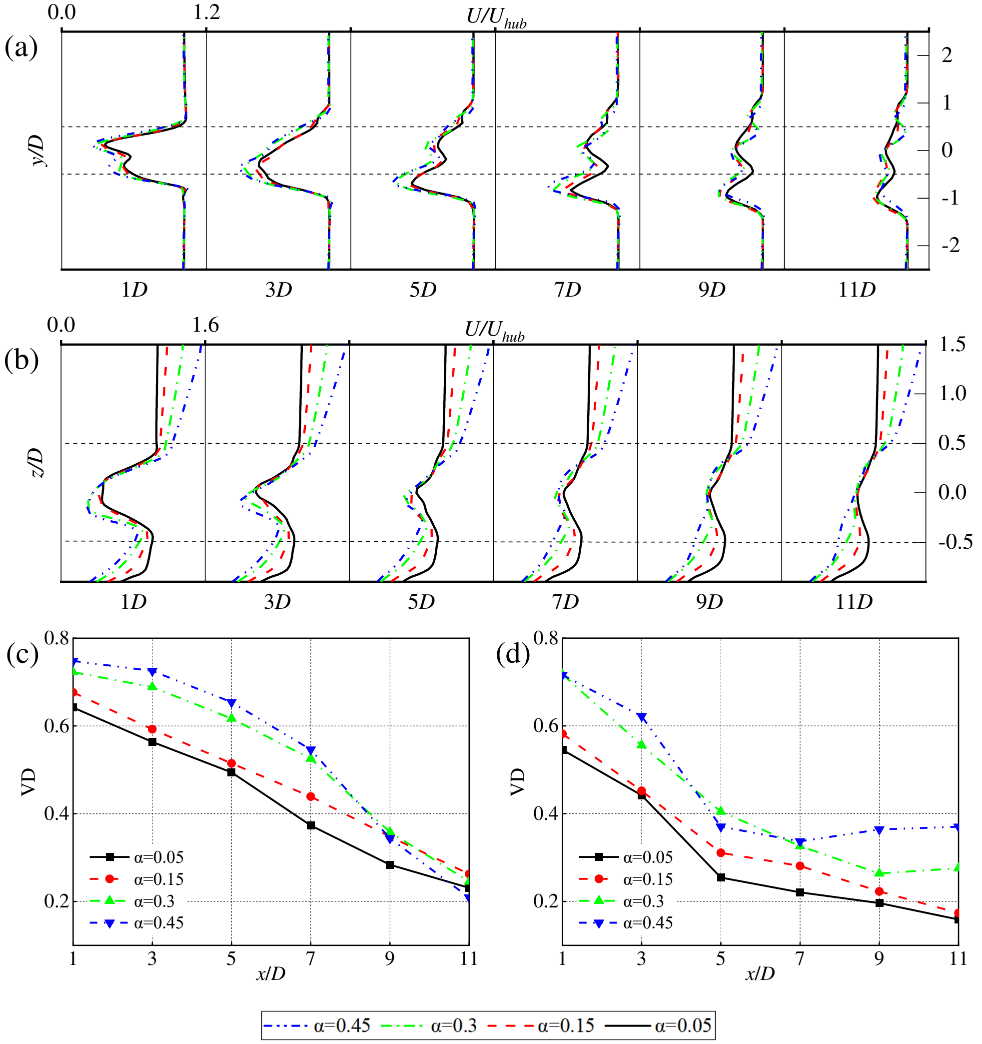

Fig. 10. Normalized mean streamwise velocity distributions under different ABL conditions (TSR = 2.19): (a) profiles in the *x*–*y* plane; (b) profiles in the *x*–*z* plane; (c) maximum velocity deficits (VD) at various downstream positions in the *x*–*y* plane; (d) maximum velocity deficits (VD) at various downstream positions in the *x*–*z* plane (-0.5 < *z*/*D* < 0.5).

As illustrated in Fig. 10(a), the wake profiles under different ABL conditions exhibit two distinct peaks. At $x = 1D$, the minimum normalized mean streamwise velocities for WSCs of 0.05, 0.15, 0.3, and 0.45 are recorded at 0.358, 0.324, 0.277, and 0.252, respectively. These findings indicate that the wake VD ($1\text{-}U/U_{hub}$) displays significant variability across ABL inflows characterized by different wind shear values. Moreover, as the downstream distance increases, the wake exhibits a skew towards the negative y-axis, a phenomenon attributed to an imbalance in momentum in the rotational direction of the blades, which is a characteristic feature of VAWTs. [33]. Additionally, ABL inflows appear to have negligible effects on the horizontal width of the wake. As shown in Fig. 10(a), the wake begins to recover with increasing downstream distance; however, even at $x = 7D$, there remains a significant divergence in wake VDs across different ABL inflow cases. Specifically, at $x = 7D$, the minimum normalized mean streamwise velocity for the case with $\alpha = 0.45$ is 0.438, which is 43.1% lower than that for the case with $\alpha = 0.05$. It is evident that the differences in wake VD for varying ABL inflow conditions gradually diminish beyond $x = 7D$. Overall, the wake profiles at varying downstream distances indicate that ABL, characterized by a higher WSC, results in a greater wake VD. Meanwhile, as the wake evolves, the influence of ABL on the distribution of wake velocity progressively attenuates.

Fig. 10(b) presents the vertical normalized mean streamwise velocity profiles of the VAWT along the midsection plane (x-z plane at $y = 0$) at specific downstream distances. The vertical wake profiles for different ABL inflow conditions exhibit non-axisymmetric characteristics, which can be attributed to the influence of wind shear present within the ABL inflow. Figs. 10(c) and 10(d) show the downstream evolution of the maximum VD, corresponding to the wake profiles presented in Figs. 10(a) and 10(b), respectively. A positive correlation between the maximum VD in the wake and the WSC is observed at downstream locations of $x = 1D$ and $x = 3D$. For example, as shown in Fig. 10(c), at $x = 3D$, the maximum VDs corresponding to WSC values of 0.05, 0.15, 0.3, and 0.45 are 0.56, 0.59, 0.69, and 0.73, respectively. However, this positive correlation evolves as the wake develops, and the trends observed in Figs. 10(c) and 10(d) are not entirely synchronous.

To facilitate a comprehensive visual analysis of the changes in the wake under varying ABL conditions, the normalized mean streamwise velocity contours are presented in Figs. 11 and 12. Fig. 11 illustrates that the horizontal cross-section of the VAWT wake exhibits a notable asymmetry, in contrast to the horizontal section of the HAWT wake. This asymmetry arises from the aforementioned Magnus effect, resulting in a significantly greater VD in the negative y-direction compared to the positive y-direction. Furthermore, the wake exhibits a faster recovery in the positive y-direction, suggesting that this orientation is more favorable for the horizontal layout design of VAWTs in this study. Although the WSC of ABLs has minimal impact on the overall structure of the wake, Figs. 11 and 12 demonstrate that the VD in the near-wake regions increases with higher WSC values. The deviation of the wake from the centerline observed in Fig. 12 is likely caused by wake meandering, an unsteady phenomenon commonly associated with wind turbine wakes.

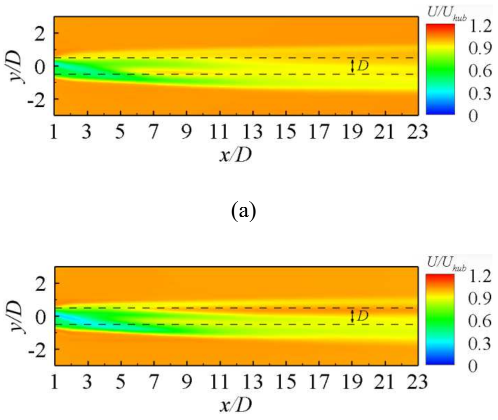

(a) (b)

(c) (d)

Fig. 11. Contours of normalized mean streamwise velocity under various ABLs (x-y plane, TSR = 2.19): (a) $\alpha = 0.05$; (b) $\alpha = 0.15$; (c) $\alpha = 0.3$; and (d) $\alpha = 0.45$.

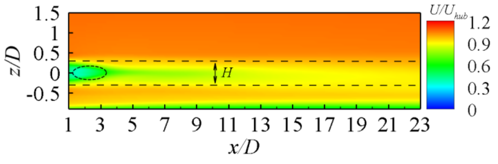

(a) (b)

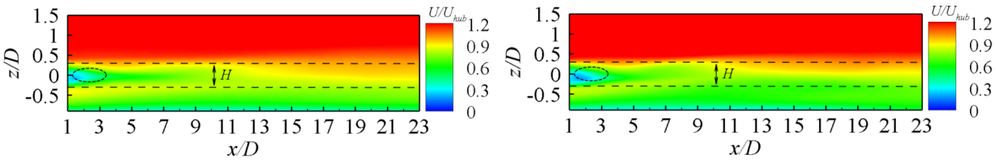

(c) (d)

Fig. 12. Contours of normalized mean streamwise velocity under various ABLs (x-z plane, TSR = 2.19): (a) $\alpha = 0.05$; (b) $\alpha = 0.15$; (c) $\alpha = 0.3$; and (d) $\alpha = 0.45$.

To intuitively illustrate the three-dimensional characteristics of wake velocity variations, Fig. 13 presents the velocity contours of the inflow and various downstream positions under different ABL conditions. The figure reveals that the distribution patterns of the near wake are quite similar across different ABL scenarios. However, as the downstream distance increases, this similarity gradually diminishes, suggesting that ABL conditions exert a limited influence on the near wake. Conversely, the effects of ABL become more pronounced in the far wake, highlighting the significance of these conditions in shaping wake dynamics at greater distances.

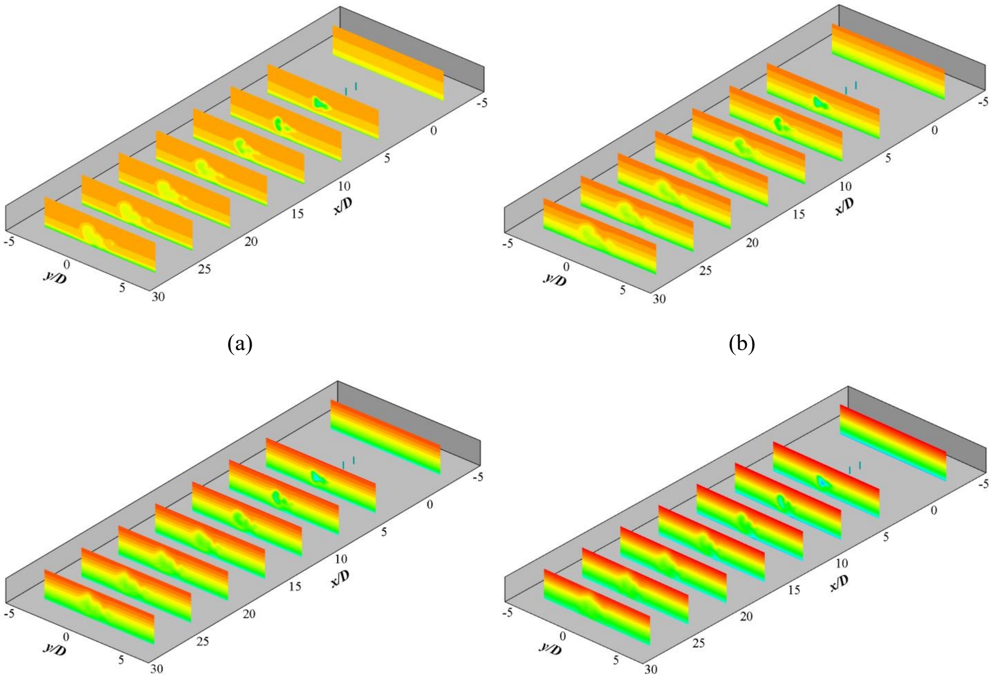

(a) (b)

(c) (d)

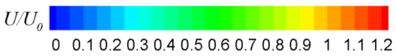

Fig. 13. Contours of normalized mean streamwise velocity at different downstream distances under various ABLs (TSR = 2.19): (a) $\alpha = 0.05$; (b) $\alpha = 0.15$; (c) $\alpha = 0.3$; and (d) $\alpha = 0.45$.

Fig. 14(a) illustrates the profiles of horizontal mean turbulent intensity (TI) of the VAWT at various downstream distances, along the midspan section in the x-y plane. TI is defined as the ratio of the root mean square of the streamwise velocity (U') to the inflow wind speed at the mid-span height of the blade (U_{hub}). Similar to the wake velocity profiles, the distribution of TI also exhibits asymmetry along the y-direction. Notably, turbulence levels in the near-wake regions are negatively correlated with the WSC. For instance, at $x = 1D$, the maximum TI values in the horizontal wake profiles for ABL conditions with WSCs of 0.05, 0.15, 0.3, and 0.45 are 15.59%, 11.83%, 7.27%, and 5.27%, respectively. Additionally, at $x = 1D$, the maximum TI is located at $y/D = 0.5$ and shows a tendency to skew towards the negative y-direction as the downstream distance increases.

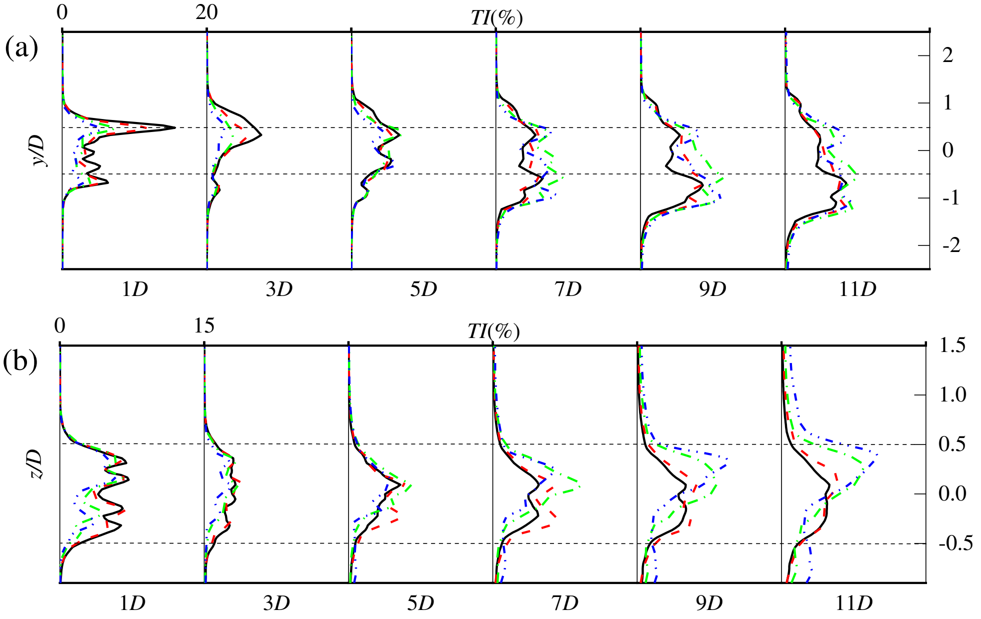

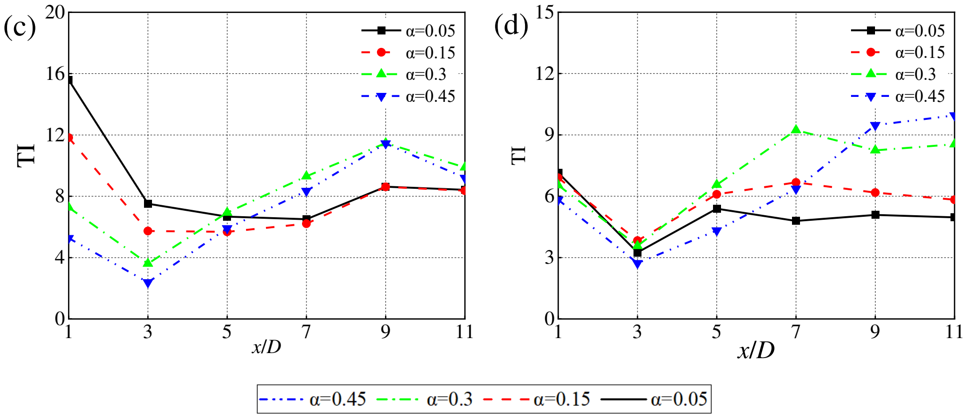

Fig. 14. Mean TI distributions under different ABL conditions (TSR = 2.19): (a) profiles in the *x*–*y* plane; (b) profiles in the *x*–*z* plane; (c) maximum TI at various downstream locations in the *x*–*y* plane; (d) maximum TI at various downstream locations in the *x*–*z* plane ($-0.5 < z/D < 0.5$).

Fig. 14(b) presents the mean TI profiles of the VAWT at various downstream distances along the midsection plane (*x-z* plane at $y = 0$). At $x = 1D$, the maximum TI of the vertical profiles exhibits a negative correlation with the WSC, consistent with the observations made in the horizontal mean TI profiles. However, this negative correlation diminishes as the downstream distance increases. Notably, at $x/D = 9$ and 11, the correlation shifts from negative to positive, with the maximum TI located in the positive z-direction. This transformation indicates a complex interaction between the turbulent intensity and wind shear as the flow develops downstream.

Figs. 14(c) and 14(d) present the statistics of the maximum TI extracted from the wake profiles shown in Figs. 14(a) and 14(b), respectively, illustrating the downstream evolution of the maximum TI. In addition to revealing how different ABL conditions affect the downstream development of TI, a distinct turning point is observed at $x/D = 3$. Notably, Peng et al. [24] identified $x/D = 2$ as the boundary between the near and far wake for a five-bladed VAWT. The emergence of this turning point in the present study potentially marks a transition from the near wake to the far wake, which appears to occur in the vicinity of $x/D = 3$. Furthermore,

Fig. 14(c) shows that between $x/D = 1$ and $x/D = 3$, cases with higher TI experience a more pronounced decrease in turbulence intensity. This observation is consistent with the findings of Kuang et al. [28], who attributed this phenomenon to the accelerated dissipation of blade-generated turbulence in more turbulent conditions. Overall, ABLs with higher WSCs tend to generate increased turbulence intensity in the far wake of the VAWT.

In addition, Figs. 15 and 16 depict the contours of the mean TI under varying ABL conditions. The results demonstrate a significant increase in TI values throughout the entire wake region with higher WSC. Overall, the presence of a strong ABL appears to significantly affect the fatigue loads on downstream VAWTs. This amplification underscores the complex interactions between wind shear and turbulent intensity in the context of wind turbine performance.

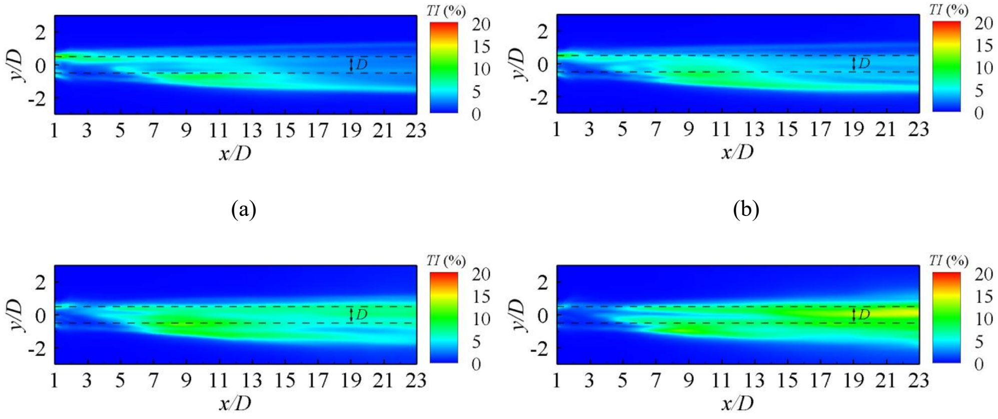

(a) (b)

(c) (d)

Fig. 15. Contours of mean TI under various ABLs (x-y plane, TSR = 2.19): (a) $\alpha = 0.05$; (b) $\alpha = 0.15$; (c) $\alpha = 0.3$; and (d) $\alpha = 0.45$.

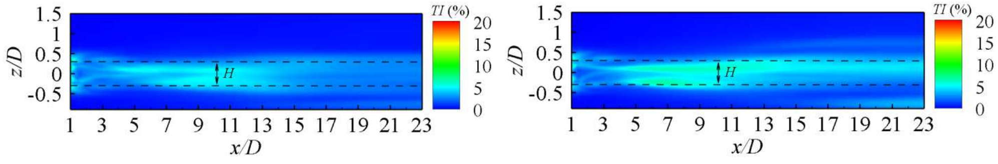

(a) (b)

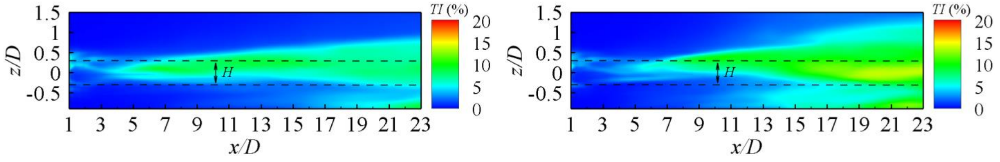

(c) (d)

Fig. 16. Contours of mean TI under various ABLs (*x*-*z* plane, TSR = 2.19): (a) $\alpha = 0.05$; (b) $\alpha = 0.15$; (c) $\alpha = 0.3$; and (d) $\alpha = 0.45$.

To achieve a more thorough understanding of the impact mechanism of the ABL on turbine wake development, the vortex structures are identified and presented in Fig. 17. These structures are identified using the Q-criterion with a threshold value of Q = 1, and the iso-surfaces are colorized based on the mean normalized streamwise velocity. The results reveal that wing-tip vortices are generated and propagate steadily downstream. Furthermore, the ABL significantly influences the stability of these vortices; under higher WSC, the breakdown of unsteady vortices occurs closer to the rotor. The colorization of the vortices reveals that large-scale vortices generated from the breakdown exhibit higher velocities. Consequently, the wake distributions of the VAWT are markedly altered under varying ABL conditions, primarily due to the substantial role of vortices in transporting momentum within the wake region. [55].

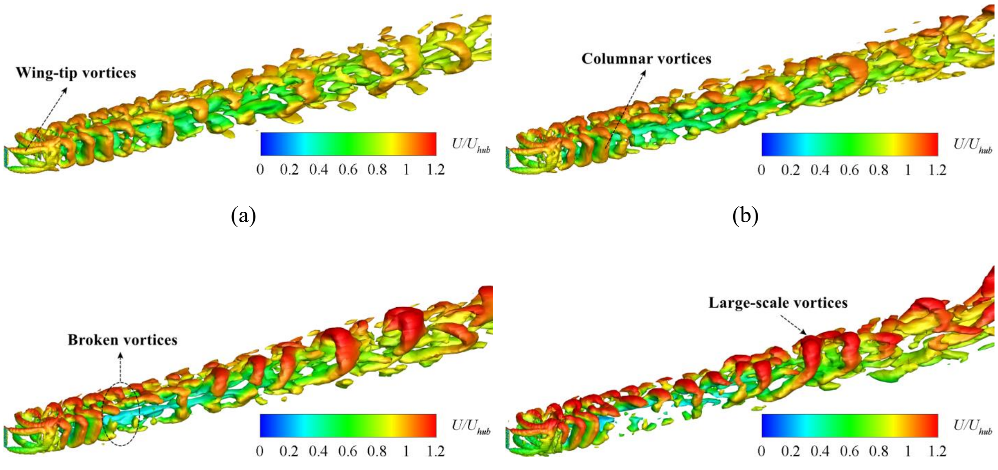

(a) (b)

(c) (d)

PLEASE CITE THIS ARTICLE AS DOI: 10.1063/5.0271326

Fig. 17. Three-dimensional vortex structures under various ABLs (TSR = 2.19): (a) $\alpha = 0.05$; (b) $\alpha = 0.15$; (c) $\alpha = 0.3$; and (d) $\alpha = 0.45$.

3.2.2 Effects of installation height

Fig. 18(a) presents the profiles of horizontal normalized mean streamwise velocity at various downstream distances for the VAWT at different installation heights. A significant divergence is observed in the wake velocity profiles corresponding to varying installation heights. Specifically, at a downstream distance of $x = 1D$, the minimum normalized mean streamwise velocities in the wake profiles for VAWTs installed at heights of $h/H = 0.5$, 1, 1.5 and 2 are 0.237, 0.277, 0.319 and 0.375, respectively. This data indicates that a VAWT installed at a greater height is capable of capturing more wind energy. However, it is important to note that this increased height does not necessarily correlate with a more pronounced VD in the wake, particularly in the near-wake regions.

Similar to the effects observed in the ABL, the installation height appears to have minimal impact on the horizontal width of the wake, with the exception of the case where $h = 0.5H$. Notably, the divergence in the wake VD for different installation heights begins to diminish gradually beyond $x = 5D$. At $x = 7D$, the minimum normalized mean streamwise velocity for the configuration with $h = 0.5H$ is measured at 0.455, which is only 13.5% lower than that of the configuration with $h = 2H$. This indicates that while installation height influences initial wake characteristics, its effect lessens at greater downstream distances.

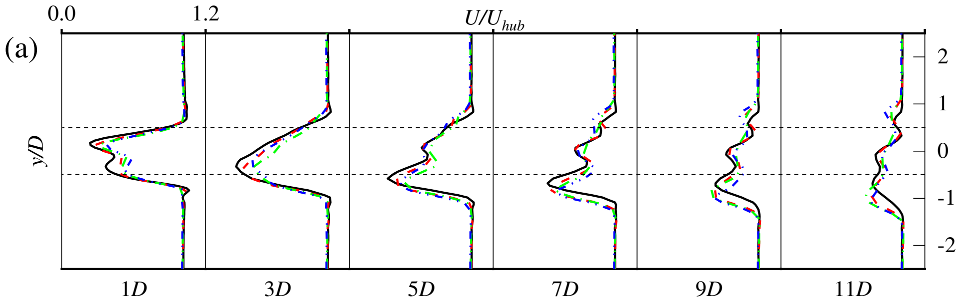

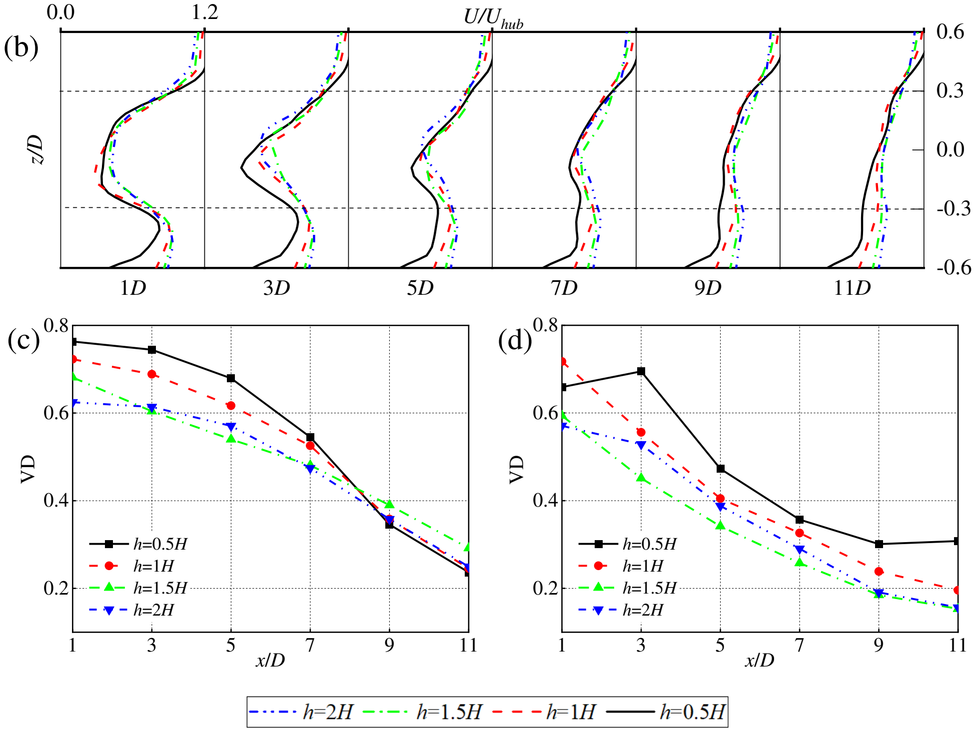

Fig. 18. Normalized mean streamwise velocity distributions under different installation heights (TSR = 2.19): (a) profiles in the *x*–*y* plane; (b) profiles in the *x*–*z* plane; (c) maximum velocity deficits (VD) at various downstream positions in the *x*–*y* plane; (d) maximum velocity deficits (VD) at various downstream positions in the *x*–*z* plane ($-0.3<z/D<0.3$).

To enhance our understanding of the wake velocity characteristics under varying installation heights, vertical normalized mean streamwise velocity profiles (*x*-*z* plane at $y = 0$) are depicted in Fig. 18(b) for selected downstream distances. For the convenience of comparison, the mid-span coordinates of blades are set to $z = 0$ for all cases with different installation heights. It can be seen from the Fig. 18(b) that the maximum VD of the wake (range is limited to blade span *H*) does not maintain a strict positive correlation with the installation height. However, the maximum VD of the cases of $h = 0.5H$ and $h = 1H$ is always greater than that of the cases of $h = 1.5H$ and $h = 2H$. Namely, the relatively higher installation height makes the wake have a lower

VD and a faster recovery. Figs. 18(c) and 18(d) present the downstream evolution of the maximum VD extracted from the wake profiles in Figs. 18(a) and 18(b), respectively. As shown in Fig. 18(c), the influence of installation height on the maximum VD becomes significantly less pronounced beyond $x/D = 5$. However, this attenuation is not observed in Fig. 18(d), suggesting that the effect of installation height on VD persists longer in the vertical direction.

Furthermore, to facilitate a comprehensive comparison of wake velocities at varying installation heights, the contours illustrating the normalized mean streamwise velocity are presented in Figs. 19 and 20. The analysis reveals that the effects of installation height on wake velocity are primarily concentrated in the regions where $x/D < 7$.

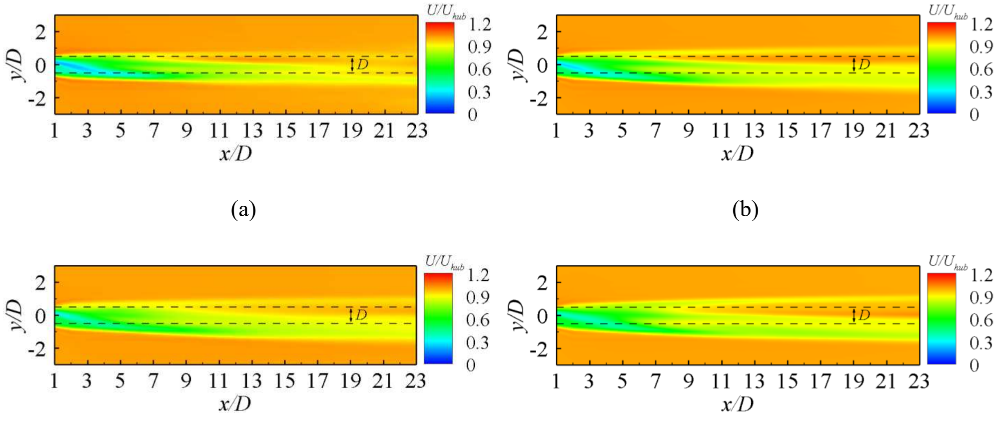

(a) (b)

(c) (d)

Fig. 19. Contours of normalized mean streamwise velocity under various installation heights (x-y plane, TSR = 2.19): (a) $h = 0.5H$; (b) $h = 1H$; (c) $h = 1.5H$; and (d) $h = 2H$.

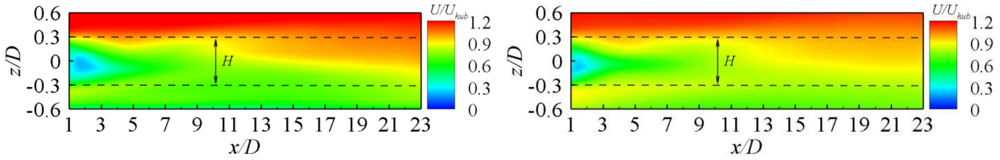

(a) (b)

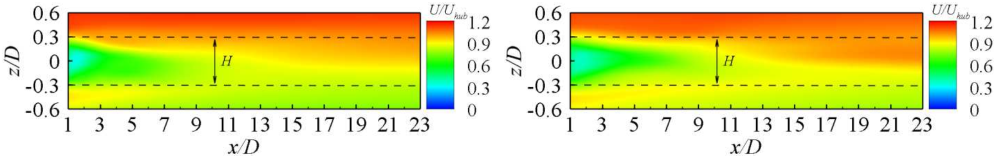

(c) (d)

Fig. 20. Contours of normalized mean streamwise velocity under various installation heights (*x*-*z* plane, TSR = 2.19): (a) $h = 0.5H$; (b) $h = 1H$; (c) $h = 1.5H$; and (d) $h = 2H$.

Fig. 21(a) depicts the mean TI profiles under various installation heights in the *x*-*y* plane. In the near wake regions, the maximum TI for the horizontal profiles is observed in the case of an installation height of $h = 1.5H$. Additionally, as the wake develops, the scenarios with relatively higher installation heights exhibit lower levels of turbulence intensity. This trend is further corroborated by the TI distribution under different installation heights, as shown in Fig. 21(b). Moreover, similar to the observations in Figs. 14(c) and 14(d), an inflection point is also identified at $x/D = 3$ in Figs. 21(c) and 21(d), indicating that installation height has no significant impact on the occurrence of this inflection point. In summary, the wake of a VAWT installed at a greater height demonstrates a faster recovery of both VD and turbulence levels.

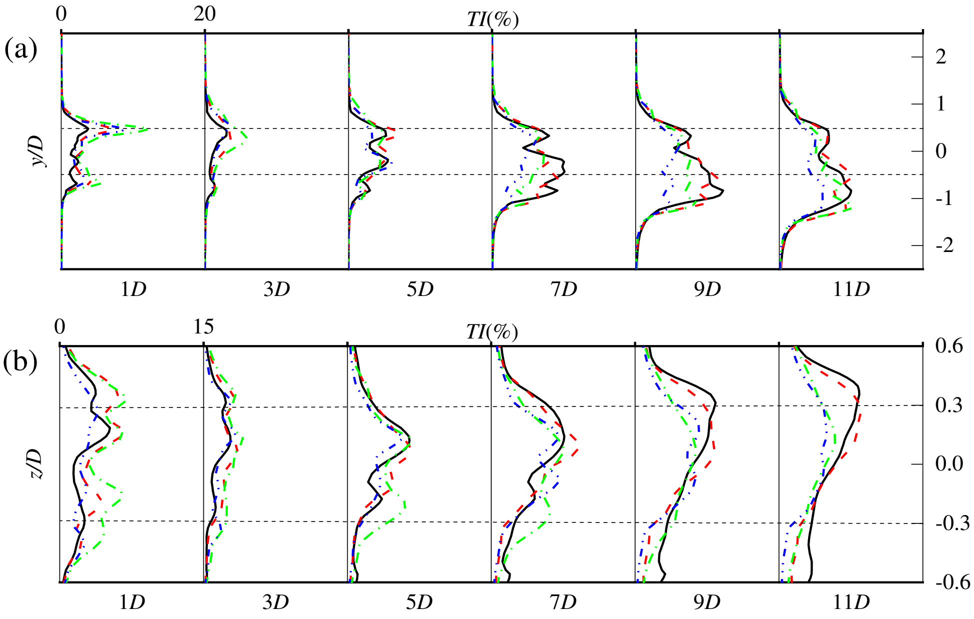

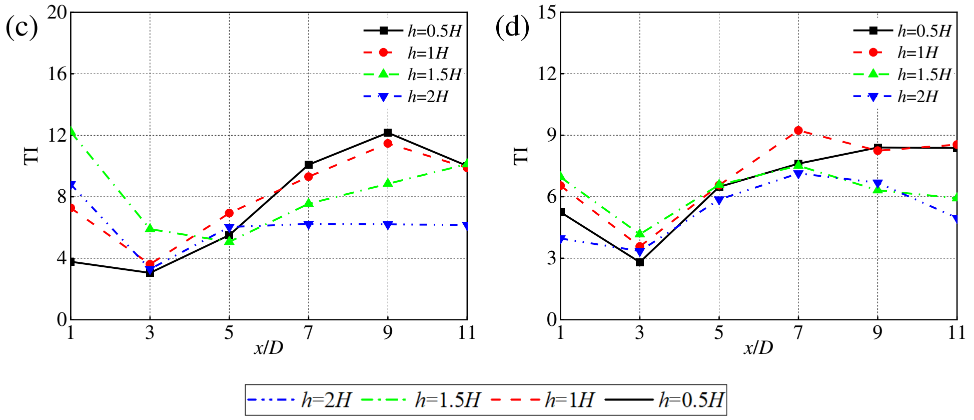

Fig. 21. Mean TI distributions under different installation heights (TSR = 2.19): (a) profiles in the *x*–*y* plane; (b) profiles in the *x*–*z* plane; (c) maximum TI at various downstream locations in the *x*–*y* plane; (d) maximum TI at various downstream locations in the *x*–*z* plane ($-0.3 < z/D < 0.3$).

The contours illustrating the mean TI at varying installation heights are presented in Figs. 22 and 23. It is evident that installation height significantly affects both the distribution and magnitude of TI within the wake. Generally, higher installation heights lead to reduced wake fluctuations, making them more suitable for positioning VAWTs downstream.

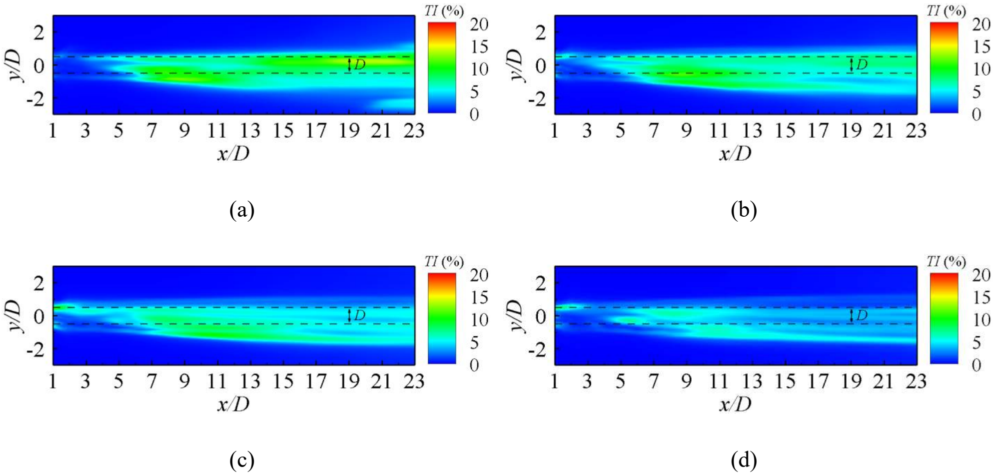

(a)

(b)

(c)

(d)

Fig. 22. Contours of mean TI under various installation heights (*x*-*y* plane, TSR = 2.19): (a) $h = 0.5H$; (b)

$h = 1H$; (c) $h = 1.5H$; and (d) $h = 2H$.

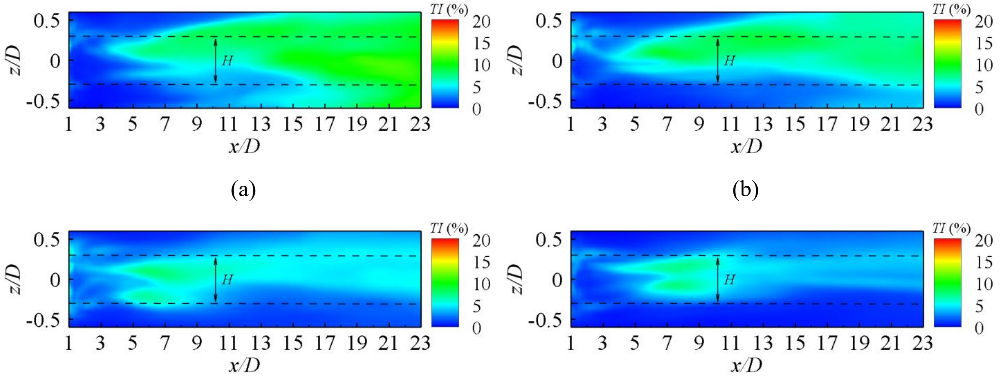

(a) (b)

(c) (d)

Fig. 23. Contours of mean TI under various installation heights (x-z plane, TSR = 2.19): (a) $h = 0.5H$; (b) $h = 1H$; (c) $h = 1.5H$; and (d) $h = 2H$.

Fig. 24 depicts the three-dimensional vortex structures corresponding to various installation heights. Vortex identification is performed using the Q-criterion, with a threshold value set at Q = 1, and the vortex is colorized based on the normalized mean streamwise velocity. A comparative analysis of wake vortices at different installation heights reveals that lower installation heights lead to an earlier onset of vortex instability. Consequently, the large-scale vortices generated by these broken vortices result in a higher turbulence level within the wake.

These observations are further supported by the corresponding TI distributions shown in Figs. 14(c), 14(d), 21(c), and 21(d), which reflect the combined effects of varying installation heights and ABL conditions. The results indicate that both factors significantly influence the evolution of wake turbulence. Specifically, distinct wind shear coefficients (WSCs) and installation heights lead to different vortex development patterns, which in turn modulate TI through mechanisms such as vortex breakdown, enhanced mixing, and energy redistribution. Notably, the divergence in TI profiles becomes prominent downstream of $x/D = 3$, suggesting that vortex breakdown predominantly occurs in the far-wake region. Around $x/D = 5$, the TI differences across cases temporarily diminish before increasing again, highlighting the dynamic and cumulative influence of vortex evolution on downstream turbulence behavior. This emphasizes the importance of considering both ABL characteristics and turbine installation height in wake dynamics studies.

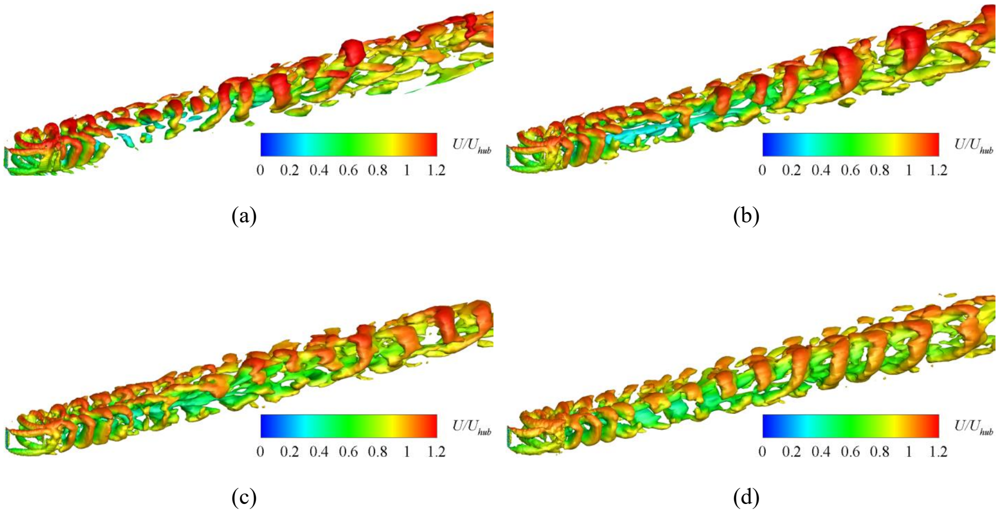

Fig. 24. Three-dimensional vortex structures under various installation heights (TSR = 2.19): (a) $h = 0.5H$; (b) $h = 1H$; (c) $h = 1.5H$; and (d) $h = 2H$.

3.3 OMD analysis

To analyze the dominant flow field structures of the VAWT under varying ABL inflow conditions, a total of 800 snapshots from the x-z plane ($y = 0$) are collected for OMD analysis. These snapshots are sampled after the flow field stabilized, with a sampling interval of T/20 (where $T = 1/f_0$, and f_0 is the rotor rotation frequency). The modal analysis revealed modes at various frequencies, each associated with specific energy levels, notably exhibiting temporal independence. The analysis of energy associated with different frequency modes indicates that modes with normalized frequencies (f/f_0) less than 1 exhibit significantly greater cumulative energy, as shown in Fig. 25(a).

Interestingly, no significant low-frequency components are observed in the spectral analysis presented in

Fig. 9. To investigate this phenomenon, we extracted and analyzed the low-frequency modes, as illustrated in Fig. 26. The corresponding modal structures reveal that these modes primarily represent the dynamic behavior in the far-wake region. This discrepancy likely arises from the fundamental differences between the two analytical approaches. The spectral analysis in Fig. 9 is based on the rotor's torque response, whereas the modal analysis captures coherent structures across the entire flow field, including the far-wake region. Since the rotor's torque response more directly influences the flow dynamics in the near-wake region and has limited impact on far-wake behavior [21], the high-energy low-frequency modes—mainly associated with the far wake—identified through modal analysis are not clearly manifested in the rotor-based spectral results.

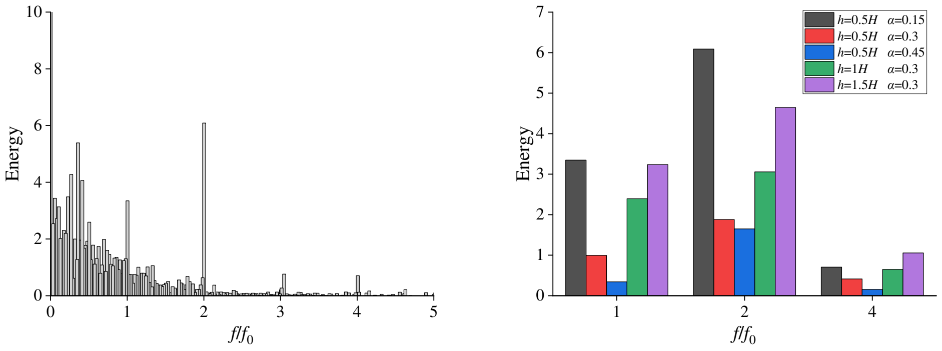

(a) (b)

Fig. 25. Energy of modes at different frequencies (TSR = 2.19): (a) $h = 0.5H$, $\alpha = 0.15$; (b) different WSCs and installation heights.

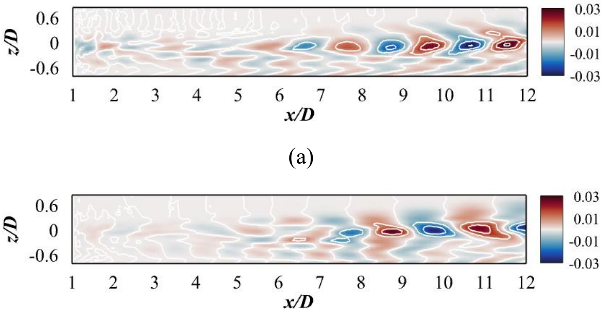

(a)

(b)

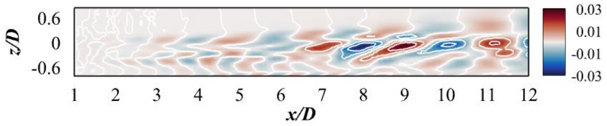

(c)

Fig. 26. Low-frequency *z*-vorticity modes at installation height $h = 0.5H$ under different wind shear coefficients (TSR = 2.19): (a) α= 0.15, (b) α= 0.3, (c) α= 0.45.

In addition to the low-frequency interharmonic modes, the mode with a normalized frequency of 2 exhibits significantly higher energy than the other modes, thereby establishing it as the dominant mode in the flow field. Fig. 25(b) presents a comparison of the energy of the streamwise velocity modes at normalized frequencies of 1, 2, and 4 across various WSC and installation heights. From this figure, it is evident that both an increase in WSC and a decrease in installation height lead to a reduction in the energy of the dominant mode. This finding underscores the influence of ABL within the blade height range on the wake structure of the VAWT.

Fig. 27 presents the modal contours of the *x*-velocity and *z*-vorticity in the wake under varying WSC. It is evident that the contour exhibits an asymmetric distribution along the z = 0 plane, with increased WSC further amplifying this asymmetry. The dynamics of the wake are closely linked to the evolution of vortices, as the figure clearly depicts the processes of vortex instability and breakdown, both of which are intensified by higher WSC. This observation aligns with the previously discussed results of the wake analysis.

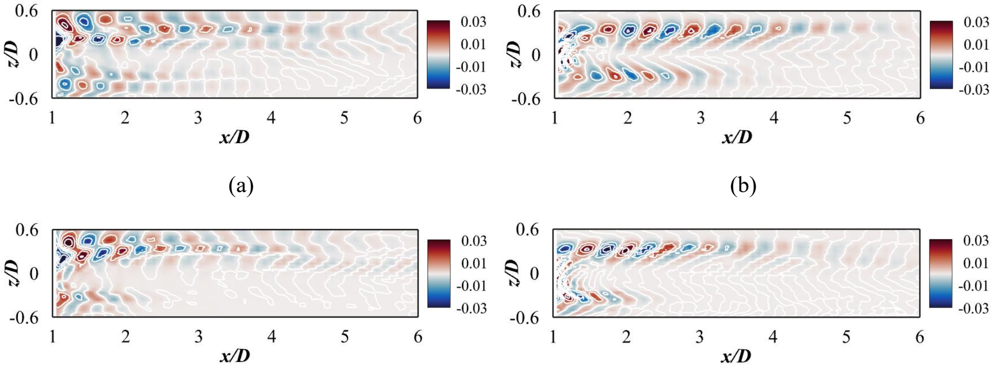

(a)

(b)

(c) (d)

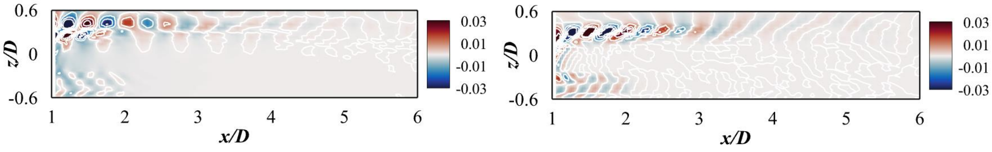

(e) (f)

Fig. 27. Contours of modes for *x*-velocity (left) and *z*-vorticity (right) under different WSCs (h = 0.5H, f/f_0 = 2, TSR = 2.19): (a), (b): α = 0.15; (c), (d): α = 0.3; (e), (f): α = 0.45.

The mechanism by which installation height affects wake characteristics is consistent with WSC, as illustrated in Fig. 28. The evolution of columnar vortices can be observed as the installation height increases. In summary, regardless of the different WSC or installation heights, the dominant modes in the wake exhibit time-varying characteristics of the vortices.

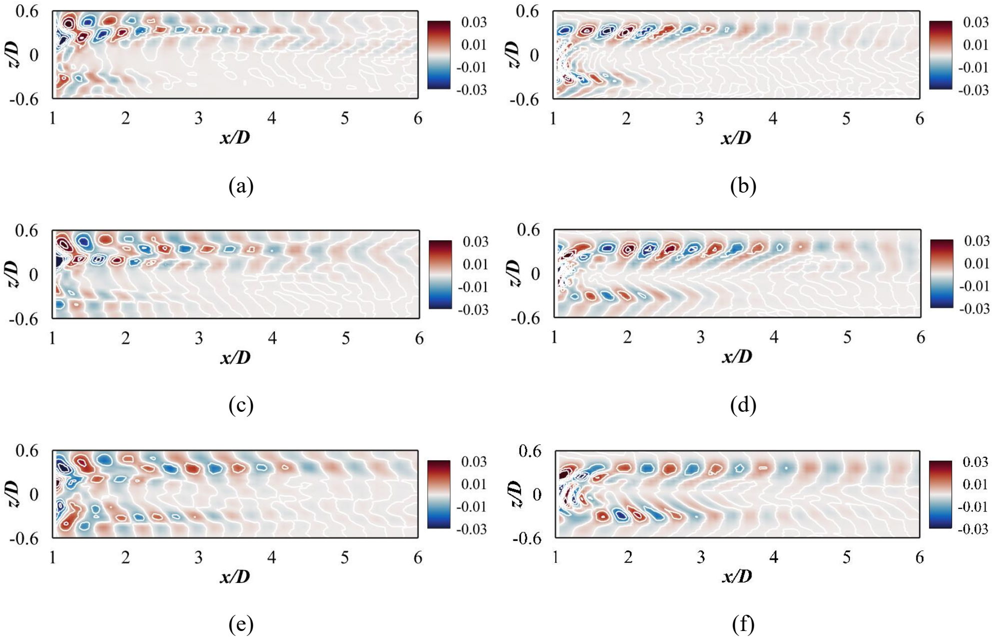

(a) (b)

(c) (d)

(e) (f)

Fig. 28. Contours of modes for *x*-velocity (left) and *z*-vorticity (right) under different installation heights (α = 0.3, f/f_0 = 2, TSR = 2.19): (a), (b): h = 0.5H; (c), (d): h = 1H; (e), (f): h = 1.5H.

4. Conclusion

The present study systematically investigates the aerodynamic performance and wake dynamics of a straight-bladed VAWT under various ABL flows. Utilizing LES, we assess the impact of ABL and installation height on power performance, wake velocity and turbulent intensity distribution. Furthermore, OMD is conducted to reveal the mechanisms by which ABL influences the VAWT wake. The primary findings of this study are summarized as follows:

(1) The aerodynamic performance of VAWTs is highly sensitive to both the ABL profile and installation height. Lower installation heights exhibit more pronounced differences in torque response across different ABLs. FFT analysis shows that both factors influence the amplitude of dominant frequency components in the torque curves.

(2) ABL profiles with higher wind shear coefficients (WSCs) lead to greater wake velocity deficits in the near-wake region. However, as the wake evolves downstream, the influence of ABL gradually weakens. Additionally, higher installation heights promote faster recovery of both velocity and turbulence intensity in the wake.

(3) ABLs with higher WSCs significantly increase turbulence intensity in the far-wake region. Furthermore, both ABL and installation height affect vortex stability: stronger shear or lower rotor placement causes earlier breakdown of wing tip and columnar vortices, generating large-scale structures that enhance turbulence levels. These unsteady flow structures can increase dynamic loading on the turbine, potentially accelerating fatigue damage and diminishing long-term operational efficiency.

(4) Modal decomposition reveals that the dominant frequency of wake structures is consistently twice the rotor rotation frequency, regardless of ABL type or installation height, highlighting the periodic and dynamic nature of wake vortex evolution.

These findings offer important insights for the practical design and optimization of VAWT wind farms.

The demonstrated sensitivity of wake characteristics and power output to ABL conditions emphasizes the necessity of integrating time-varying ABL evaluations into wind farm planning and siting strategies. Additionally, the observed influence of installation height on wake recovery and turbulence distribution highlights the critical role of hub height optimization in achieving an effective trade-off between maximizing energy production and minimizing wake-induced interference within turbine arrays.

This study has certain limitations, such as not considering the wake interference of VAWTs in tandem arrangements. As demonstrated by Kuang et al. [28], the enhanced turbulence intensity in the wake of upstream turbines can supply additional momentum and energy to downstream units. However, conducting high-fidelity simulations of large-scale tandem VAWT configurations poses significant computational challenges. Future research could focus on developing efficient reduced-order modeling frameworks to systematically explore the impact of atmospheric boundary layer (ABL) conditions on array effects, thereby supporting the optimization of VAWT wind farm layouts. Additionally, in offshore wind farms, the pitch motion of platforms is an important factor to consider. Developing relevant wake analysis models is also a noteworthy research direction.

Acknowledgements

The authors gratefully appreciate the financial support provided by the National Natural Science Foundation of China (Grant No. 51908107).

Author Declarations

Conflict of Interest

The authors have no conflicts to disclose.

Data availability

The data that support the findings of this study are available from the corresponding authors upon reasonable request.

References

[1] Zhao F, Mumtaz Qadri MN, Wang Z, Tang H. Flow-energy harvesting using a fully passive flapping foil: A guideline on design and operation. International Journal of Mechanical Sciences. 2021;197:106323.

[2] Zhao F, Jiang Q, Wang Z, Qadri MNM, Li L, Tang H. Interaction of two fully passive flapping foils arranged in tandem and its influence on flow energy harvesting. Energy. 2023;268:126714.

[3] Zhao F, Wang Z, Bai H, Tang H. Energy harvesting based on flow-induced vibration of a wavy cylinder coupled with tuned mass damper. Energy. 2023;282:128584.

[4] Zhao F, Wang Z, Qadri MNM, Khan O, Munir A, Shahzad A, et al. Effects of wake interaction on energy extraction performance of tandem semi-active flapping foils. Physics of Fluids. 2023;35(8):087112.

[5] Zhang H, Wen J, Zhan J, Xin D. Effects of blade number on the aerodynamic performance and wake characteristics of a small horizontal-axis wind turbine. Energy Conversion and Management. 2022;273:116410.

[6] Lu H, Zhou L, Wen J, Tang H, Guo P, Tse TKT, et al. Aerodynamic performance improvements for a Savonius turbine above a forward-facing step via inclined solar panel: A computational study. Journal of Cleaner Production. 2023;413:137413.

[7] Wen J, Zhou L, Zhang H. Mode interpretation of blade number effects on wake dynamics of small-scale horizontal axis wind turbine. Energy. 2023;263:125692.

[8] Zhou L, Wen J, Wang Z, Deng P, Zhang H. High-fidelity wind turbine wake velocity prediction by surrogate model based on d-POD and LSTM. Energy. 2023;275:127525.

[9] Yue H, Zhang H, Zhu Q, Ai Y, Tang H, Zhou L. Wake dynamics of a wind turbine under real-time varying inflow turbulence: A coherence mode perspective. Energy Conversion and Management. 2025;332:119729.

[10] Ismail MF, Vijayaraghavan K. The effects of aerofoil profile modification on a vertical axis wind turbine performance. Energy. 2015;80:20-31.

[11] Zhao Z, Wang D, Wang T, Shen W, Liu H, Chen M. A review: Approaches for aerodynamic performance improvement of lift-type vertical axis wind turbine. Sustainable Energy Technologies and Assessments. 2022;49:101789.

[12] Zhang L, Li Y, Xu W, Gao Z, Fang L, Li R, et al. Systematic analysis of performance and cost of two floating offshore wind turbines with significant interactions. Applied Energy. 2022;321:119341.

[13] Hand B, Cashman A. A review on the historical development of the lift-type vertical axis wind turbine: From onshore to offshore floating application. Sustainable Energy Technologies and Assessments. 2020;38:100646.

[14] Rezaeiha A, Montazeri H, Blocken B. Characterization of aerodynamic performance of vertical axis wind turbines: Impact of operational parameters. Energy Conversion and Management. 2018;169:45-77.

[15] Chen W-H, Chen C-Y, Huang C-Y, Hwang C-J. Power output analysis and optimization of two straight-bladed vertical-axis wind turbines. Applied Energy. 2017;185:223-32.

[16] Kuang L, Katsuchi H, Zhou D, Chen Y, Han Z, Zhang K, et al. Strategy for mitigating wake interference between offshore vertical-axis wind turbines: Evaluation of vertically staggered arrangement. Applied Energy. 2023;351:121850.

[17] Paulsen US, Madsen HA, Hattel JH, Baran I, Nielsen PH. Design Optimization of a 5 MW Floating Offshore Vertical-axis Wind Turbine. Energy Procedia. 2013;35:22-32.

[18] Barthelmie RJ, Hansen K, Frandsen ST, Rathmann O, Schepers JG, Schlez W, et al. Modelling and measuring flow and wind turbine wakes in large wind farms offshore. Wind Energy. 2009;12(5):431-44.

[19] Borg M, Shires A, Collu M. Offshore floating vertical axis wind turbines, dynamics modelling state of the art. part I: Aerodynamics. Renewable and Sustainable Energy Reviews. 2014;39:1214-25.

[20] Kinzel M, Mulligan Q, Dabiri JO. Energy exchange in an array of vertical-axis wind turbines. Journal of Turbulence. 2012;13:N38.

[21] Vermeer LJ, Sørensen JN, Crespo A. Wind turbine wake aerodynamics. Progress in Aerospace Sciences. 2003;39(6):467-510.

[22] Peng HY, Liu HJ, Yang JH. A review on the wake aerodynamics of H-rotor vertical axis wind turbines. Energy. 2021;232:121003.

[23] Tescione G, Ragni D, He C, Simão Ferreira CJ, van Bussel GJW. Near wake flow analysis of a vertical axis wind turbine by stereoscopic particle image velocimetry. Renewable Energy. 2014;70:47-61.

[24] Peng HY, Lam HF, Lee CF. Investigation into the wake aerodynamics of a five-straight-bladed vertical axis wind turbine by wind tunnel tests. Journal of Wind Engineering and Industrial Aerodynamics. 2016;155:23-35.

[25] Araya DB, Colonius T, Dabiri JO. Transition to bluff-body dynamics in the wake of vertical-axis wind turbines. Journal of Fluid Mechanics. 2017;813:346-81.

[26] Posa A. Wake characterization of paired cross-flow turbines. Renewable Energy. 2022;196:1064-94.

[27] Posa A, Parker CM, Leftwich MC, Balaras E. Wake structure of a single vertical axis wind turbine. International Journal of Heat and Fluid Flow. 2016;61:75-84.

[28] Kuang L, Lei H, Zhou D, Han Z, Bao Y, Zhao Y. Numerical Investigation of Effects of Turbulence Intensity on Aerodynamic Performance for Straight-Bladed Vertical-Axis Wind Turbines. Journal of Energy Engineering. 2021;147(1):04020087.

[29] Syed Ahmed Kabir IF, Ng EYK. Effect of different atmospheric boundary layers on the wake characteristics of NREL phase VI wind turbine. Renewable Energy. 2019;130:1185-97.

[30] Porté-Agel F, Wu Y-T, Lu H, Conzemius RJ. Large-eddy simulation of atmospheric boundary layer flow through wind turbines and wind farms. Journal of Wind Engineering and Industrial Aerodynamics. 2011;99(4):154-68.

[31] Li T, Liu Z, Wang H, Bian W, Yang Q. Large eddy simulation for the effects of ground roughness and atmospheric stratification on the wake characteristics of wind turbines mounted on complex terrains. Energy Conversion and Management. 2022;268:115977.

[32] Dou B, Guala M, Zeng P, Lei L. Experimental investigation of the power performance of a minimal wind turbine array in an atmospheric boundary layer wind tunnel. Energy Conversion and Management. 2019;196:906-19.

[33] Kadum H, Friedman S, Camp EH, Cal RB. Development and scaling of a vertical axis wind turbine wake. Journal of Wind Engineering and Industrial Aerodynamics. 2018;174:303-11.

[34] Rolin VFC, Porté-Agel F. Experimental investigation of vertical-axis wind-turbine wakes in boundary layer flow. Renewable Energy. 2018;118:1-13.

[35] Hohman TC, Martinelli L, Smits AJ. The effects of inflow conditions on vertical axis wind turbine wake structure and performance. Journal of Wind Engineering and Industrial Aerodynamics. 2018;183:1-18.

[36] Tian L, Song Y, Zhao N, Shen W, Wang T, Zhu C. Numerical investigations into the idealized diurnal cycle of atmospheric boundary layer and its impact on wind turbine's power performance. Renewable Energy. 2020;145:419-27.

[37] Lin J, Xu Y-l, Xia Y. Structural Analysis of Large-Scale Vertical Axis Wind Turbines Part II: Fatigue and Ultimate Strength Analyses.   Energies2019.

[38] Lin J, Xu Y-L, Xia Y, Li C. Structural Analysis of Large-Scale Vertical-Axis Wind Turbines, Part I: Wind Load Simulation.   Energies2019.

[39] Li Qa, Maeda T, Kamada Y, Murata J, Furukawa K, Yamamoto M. Effect of number of blades on aerodynamic forces on a straight-bladed Vertical Axis Wind Turbine. Energy. 2015;90:784-95.

[40] Bangga G, Dessoky A, Lutz T, Krämer E. Improved double-multiple-streamtube approach for H-Darrieus vertical axis wind turbine computations. Energy. 2019;182:673-88.

[41] Dessoky A, Bangga G, Lutz T, Krämer E. Aerodynamic and aeroacoustic performance assessment of H-rotor darrieus VAWT equipped with wind-lens technology. Energy. 2019;175:76-97.

[42] Dessoky A, Lutz T, Bangga G, Krämer E. Computational studies on Darrieus VAWT noise mechanisms employing a high order DDES model. Renewable Energy. 2019;143:404-25.

[43] Lei H, Su J, Bao Y, Chen Y, Han Z, Zhou D. Investigation of wake characteristics for the offshore floating vertical axis wind turbines in pitch and surge motions of platforms. Energy. 2019;166:471-89.

[44] Lei H, Zhou D, Bao Y, Li Y, Han Z. Three-dimensional Improved Delayed Detached Eddy Simulation of a two-bladed vertical axis wind turbine. Energy Conversion and Management. 2017;133:235-48.

[45] Lei H, Zhou D, Lu J, Chen C, Han Z, Bao Y. The impact of pitch motion of a platform on the aerodynamic performance of a floating vertical axis wind turbine. Energy. 2017;119:369-83.

[46] Zhang Y, Li Qa, Zhu X, Song X, Cai C, Zhou T, et al. Effect of the bionic blade on the flow field of a straight-bladed vertical axis wind turbine. Energy. 2022;258:124834.

[47] Mo JO, Choudhry A, Arjomandi M, Kelso R, Lee YH. Effects of wind speed changes on wake instability of a wind turbine in a virtual wind tunnel using large eddy simulation. Journal of Wind Engineering and Industrial Aerodynamics. 2013;117:38-56.

[48] Sedaghatizadeh N, Arjomandi M, Kelso R, Cazzolato B, Ghayesh MH. Modelling of wind turbine wake using large eddy simulation. Renewable Energy. 2018;115:1166-76.

[49] Li Qa, Maeda T, Kamada Y, Murata J, Yamamoto M, Ogasawara T, et al. Study on power performance for straight-bladed vertical axis wind turbine by field and wind tunnel test. Renewable Energy. 2016;90:291-300.

[50] Qiao L, Zhao Y, Zhou L, Ai Y, Zhu Q, Zhang H. Coherence mode and Floquet analysis on flow past a rectangular cylinder with small angle of attack. Physics of Fluids. 2024;36(12):123616.

[51] He Z, Zhao Y, Zhang H, Tang H, Zhu Q, Ai Y, et al. Vortex-induced vibrations and galloping of a square cylinder: The impact of damping and mass ratio. Ocean Engineering. 2025;320:120371.

[52] Zhou L, Noack BR, Tse KT, He X. Interpretation and prediction of the three-dimensional coherent structure and its dynamics of tornado-like vortex via delayed proper orthogonal decomposition. Physics of Fluids. 2025;37(1):013106.

[53] Wynn A, Pearson DS, Ganapathisubramani B, Goulart PJ. Optimal mode decomposition for unsteady flows. Journal of Fluid Mechanics. 2013;733:473-503.

[54] Swanson WM. The Magnus Effect: A Summary of Investigations to Date. Journal of Basic Engineering. 1961;83(3):461-70.

[55] Lei H, Zhou D, Bao Y, Chen C, Ma N, Han Z. Numerical simulations of the unsteady aerodynamics of a floating vertical axis wind turbine in surge motion. Energy. 2017;127:1-17.